Deformation of Elastomeric Networks: Relation between Molecular Level Deformation and Classical Statistical Mechanics Models of Rubber Elasticity

J. S. Bergström† and M. C. Boyce*

Department of Mechanical Engineering, Massachusetts Institute of Technology, Cambridge, Massachusetts 02139

Received May 8, 2000; Revised Manuscript Received October 16, 2000

ABSTRACT: In this work, molecular simulations are conducted to provide details of the underlying micromechanisms governing the observed macroscopic behavior of elastomeric materials. The polymer microstructure is modeled as a collection of unified atoms interacting by two-body potentials of bonded and nonbonded type. Representative volume elements (RVEs) containing a network of 200 molecular chains of 100 bond lengths are constructed. The evolution of the RVEs with uniaxial deformation was studied using a molecular dynamics technique. The simulations enable observation of structural features with deformation including bond lengths and angles as well as chain lengths and angles. The simulations also enable calculation of the macroscopic stress−strain behavior and its decomposition into bonded and nonbonded contributions. The distribution in initial end-to-end chain lengths is consistent with Gaussian statistics treatments of rubber elasticity. It is shown that application of an axial strain of ±0.7 (a logarithmic strain measure is used) only causes a change in the average bond angle of ±5°, indicating the freedom of bonds to sample space at these low to moderate deformations; the same strain causes the average chain angle to change by ±20°. Randomly selected individual chains are monitored during deformation; their individual chain lengths and angles are found to evolve in an essentially affine manner consistent with Gaussian statistics treatments of rubber elasticity. The average chain length and angle are found to evolve in a manner consistent with the eight-chain network model of rubber elasticity. Energy quantities are found to remain constant during deformation consistent with the nature of rubber elasticity being entropic in origin. The stress−strain response is found to have important bonded and nonbonded contributions. The bonded contributions arise from the rotations of the bonds toward the maximum principal stretch axis(es) in tensile (compressive) loading.

1. Introduction

The macromolecular network structure of elastomeric materials provides the ability of these materials to undergo large strain, nonlinear elastic deformations. The underlying structure is essentially one of long, randomly oriented molecular chains in a network arrangement due to sparse cross-linking between the long chain molecules; furthermore, the intermolecular interactions are weak. The nature of this structure results in a stress−strain behavior that is governed by changes in configurational entropy as the randomly oriented molecular network becomes preferentially oriented with stretching. The essence of this behavior has been well-modeled by statistical mechanics treatments of rubber elasticity (for example, see Treloar[1] for a review). In this work, we first provide a brief review of a few selected models of rubber elastic deformation for purpose of later comparison, and we then present a molecular dynamics (MD) simulation of an elastomeric network and its deformation. The MD simulation provides detailed insight into the initial molecular network structure as well as the evolution of the network with deformation and the resulting stress−strain behavior. The relationships between the structural evolution observed in the MD simulations and that predicted by classical statistical mechanics models of rubber elasticity are also discussed.

† Currently at Exponent, Inc., Natick, MA 01760.

2. Statistical Mechanics Constitutive Models

An excellent review of the development of statistical mechanics treatments of rubber elasticity is given in Treloar.[1] Here a cursory review is provided for the purpose of later comparisons. The statistical mechanics approach begins by assuming a structure of randomly oriented long molecular chains. In the Gaussian treatment[2,3] the distribution of the end-to-end length, l, of a chain is given by $P(l)$: where n is the number of links in

$$P(l) = 4\pi\left(\frac{3}{2\pi nb^2}\right)^{3/2} l^2 \exp\left(-\frac{3l^2}{2nb^2}\right) \tag{1}$$

the chain and b is the length of each link. The average initial chain length, l_0, is given by the root-mean-square value of l:

$$l_0 = \langle l^2 \rangle^{1/2} = b\sqrt{n} \tag{2}$$

When deformation is applied, the chain structure stretches. If one considers the deformation of an assembly of N_c chains per unit reference volume by a principal stretch state (λ_1, λ_2, λ_3) and the deformation is such that the chain length l does not approach its fully extended length $l_{max} = nb$, then the elastic strain energy density function, W, can be derived from the change in configurational entropy:

$$W = \frac{1}{2} N_c k_B \theta (\lambda_1^2 + \lambda_2^2 + \lambda_3^2 - 3) \tag{3}$$

10.1021/ma0007942 CCC: $20.00
Published on Web 12/28/2000

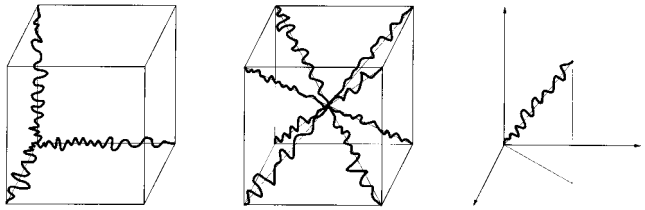

Figure 1. Different chain topologies: (a) three-chain; (b) eight-chain; (c) full network.

where k_B is Boltzmann's constant and θ is the absolute temperature. The stress−stretch relationship is then found by differentiating the strain energy density function.

The derivation of eq 3 relies on $l \ll nb$. At deformations where l begins to approach the fully extended length, the non-Gaussian nature of the chain stretch must be taken into account. Kuhn and Grün[4] accounted for the finite extensibility of chain stretch using Langevin chain statistics. To incorporate these more accurate chain statistics into a constitutive framework, it is necessary to have a model that relates the chain stretch to the applied deformation; this is accomplished by assuming a representative network structure. Three network models are shown in Figure 1.

The unit cell used in each of these models is taken to deform in principle stretch space; the models differ in how the deformation of the chains is related to the deformation of the unit cell. In the "three-chain" model,[5] the chains are located along the axes of the cell; in the "eight-chain" model,[6] the chains are located along the diagonals of the unit cell; and in the full-network or total assembly of chains model,[7,8] the chains are assumed to be randomly distributed in space and all chains are taken to deform in an affine manner. Of these models, the eight-chain representation appears to give the best predictions when compared to experimental data.[6,8] The strain energy density for the Arruda−Boyce eight-chain model (assuming incompressibility) is given by

$$W = N_c k\theta \sqrt{n}\left[\beta\lambda_{chain} - \sqrt{n}\ln\left(\frac{\sinh\beta}{\beta}\right)\right] \tag{4}$$

where

$$\lambda_{chain} = \sqrt{\frac{1}{3}(\lambda_1^2 + \lambda_2^2 + \lambda_3^2)} \tag{5}$$

$$\beta = L^{-1}\left(\frac{\lambda_{chain}}{\sqrt{n}}\right) \tag{6}$$

where λ_{chain} is the stretch in each chain in the network and $L^{-1}(x)$ is the inverse Langevin function that can be estimated from

$$L^{-1}(x) = \begin{cases} 1.31446\tan(1.58986x) + 0.91209x, & \text{if } |x| < 0.84136, \\ 1/(\sin(x) - x), & \text{if } 0.84136 \le |x| < 1 \end{cases} \tag{7}$$

We note that these models capture the equilibrium behavior of rubber elastic materials. The nonequilibrium behavior results in the time-dependent and hysteretic behavior of elastomers. Constitutive models have also been proposed for the nonequilibrium behavior (see, for example, Bergstrom and Boyce[9]).

The success of the statistical mechanics models of rubber elasticity can now be explored in detail using molecular level modeling. Below, simulation of the structure and the deformation of an elastomeric network are presented; results are compared to the models presented above where possible.

3. Molecular Model Description

One of the most important choices when developing a molecular simulation code is the decision of what potential energies to use. To a large extent the physical behavior of a material is governed by the nature of the interatomic interaction, by the potential energies of the interactions. When one is studying the mechanical properties of a polymeric material, however, the behavior is mainly governed by the topological features of the microstructure such as network structure and entanglements, and using a coarse graining procedure can therefore be a successful approach. To optimize the simulation code for speed, it is desirable to use potential energies that are as simple as possible, while still keeping the necessary chainlike features of the polymer microstructure. In this work the focus is on cross-linked polymeric systems above the glass transition temperature; the behavior of glassy polymers using similar techniques has recently been studied by Chui and Boyce.[10] Gao and Weiner[11,12] have also used a similar approach on much simpler chain systems to study the role of nonbonded interactions on rubber elasticity theory. Above the glass transition temperature, the thermal energy is high, and it is possible to neglect the energy associated with bond angle rotations and torsions. It is therefore sufficient to use simple bonded and nonbonded potentials when representing the microstructure, as also done in Gao and Weiner.[11,12] Therefore, in some sense, the chain can be considered "freely jointed"; however, the model presented here does account for bond stretching and Lennard−Jones interactions, and in its strictest sense, the freely jointed chain has fixed bond lengths and no restrictions on bond or torsion angles.[22] The bonded potential is here taken as a linear harmonic spring

$$U_B^{tot} = \sum_{\alpha\in b}\frac{c_B}{2}[r_\alpha - b]^2 \tag{8}$$

where the sum is over all bonds α, c_B is the spring stiffness, b the bond length at zero force, and r_α the length of bond α. The interchain potential is represented with a shifted and truncated Lennard−Jones potential[23]

$$U_{LJ}^{tot} = \sum_{\alpha\in nb} U_{LJ}(r_\alpha) \tag{9}$$

where the sum is over all pairs of atoms α, unless the pair of atoms are nearest chain neighbors, and where

$$U_{LJ}(r_\alpha) = \begin{cases} 4\epsilon_{LJ}\left[\left(\frac{\Lambda}{r_\alpha}\right)^{12} - \left(\frac{\Lambda}{r_\alpha}\right)^{6} - \left(\frac{1}{r_c}\right)^{12} + \left(\frac{1}{r_c}\right)^{6}\right], & \text{if } r_\alpha < r_c\Lambda \\ 0 & \text{otherwise} \end{cases} \tag{10}$$

In eq 10, ϵ_{LJ} is the Lennard−Jones potential strength, r_c is the cutoff distance, Λ is the excluded volume parameter, and $r_c\Lambda$ is the interaction distance.

In molecular simulations, computation time is dominated by the calculation of the potential energies or gradients of the potential energies. Direct computation of these terms scale as N^2, where N is the number of atoms. To minimize the computational effort, a cutoff distance, r_c, is implemented such that all interactions at $r > r_c$ are ignored. Different techniques can be used to monitor which atoms are within the cutoff distance. The two techniques used here are the Verlet neighbor list[13] and the link-cell method.[14]

In molecular simulations, it is often convenient to express quantities in reduced units. This means that a convenient set of base variables is chosen and then all other quantities are normalized with respect to these base variables. A natural choice for base variables in this case is as follows: m (atom mass), θ (temperature), b (bond length), and k_B (Boltzmann's constant). Normalized base units can then be written

$$[\text{energy}] \triangleq k_B\theta \tag{11}$$

$$[\text{force}] \triangleq \frac{k_B\theta}{b} \tag{12}$$

$$[\text{time}] \triangleq \sqrt{\frac{mb^2}{k_B\theta}} \tag{13}$$

$$[\text{velocity}] \triangleq \sqrt{\frac{k_B\theta}{m}} \tag{14}$$

$$[\text{acceleration}] \triangleq \frac{k_B\theta}{mb} \tag{15}$$

Reduced variables, denoted with a tilde, can then be expressed in terms of these reduced base units, e.g., $\tilde{c}_b = \tilde{c}_b(k_b\theta/b^2)$. The most important reason for introducing reduced units is that infinitely many combinations of the input variables correspond to the same state in terms of reduced units.

The cross-linking procedure used in this work is similar to that used by Duering.[15] First, a melt of linear monodispersed chains is generated and reactive tetrafunctional groups added to all chain ends. The network structure is then generated by running an initial Monte Carlo based cross-linking step during which chain ends that are within a predefined distance from each other are permanently attached. To further speed up the cross-linking step an artificial potential energy is introduced between all chain ends

$$U_{CL}^{tot} = \sum_{\alpha \in ce} U_{CL}(r_\alpha) \tag{16}$$

where the sum is over all pairs of chain ends and where

$$U_{CL}(r_\alpha) = \frac{-K_{CL}\phi}{r_\alpha} \tag{17}$$

The constant K_{CL} determines the strength of the cross-linking potential, and ϕ is 1 if the sum of the current functionalities of the two chain ends is less than or equal to 4 and ϕ is −1 otherwise. In some simulations, both the reduced density and the temperature were increased to further facilitate the cross-linking procedure.

Calculation of stresses can be accomplished with the virial stress theorem from statistical mechanics (for example, Gao and Weiner[11]). For a system of atoms interacting with two-body potentials, the Cauchy stress is given by[24]

$$VT_{ij} = -Nk_B\theta\delta_{ij} + \sum_{\alpha \in b}\left\langle \frac{r_{\alpha i}r_{\alpha j}}{r_\alpha}\frac{\partial U_B^{tot}}{\partial r_\alpha}\right\rangle + \sum_{\alpha \in nb}\left\langle \frac{r_{\alpha i}r_{\alpha j}\partial U_{LJ}^{tot}}{r_\alpha \quad \partial r_\alpha}\right\rangle \tag{18}$$

where V is the volume of the RVE, N is the number of atoms in the RVE, r_α is the distance between the pair of atoms α, $r_{\alpha i}$ is the ith component of r_α, and $\langle\cdot\rangle$ represent ensemble or time average. Using eq 18 the stresses in the three axial directions can be calculated. In $NV\theta$ simulations (often called NVT simulations, but T is here used to symbolize Cauchy stress), the volume is held constant, which can give rise to a pressure. Therefore, in incompressible uniaxial deformation the stresses also contain a pressure contribution, i.e. this hydrostatic stress needs to be taken into account giving the axial stress as $\sigma = T_{xx} - {}^1/_2(T_{yy} + T_{zz})$.

Once the initial network structure and the potential energies have been specified, the prescribed boundary displacements can be applied. A number of different techniques can be used to apply the deformation; in this work, a molecular dynamics algorithm has been employed. The details of this approach are described in the next subsection.

3.1. Molecular Dynamics Algorithm. The MD simulations consider a canonical ensemble (N,V,θ). The (N,V,θ) ensemble necessitates a modification of the equations of motion with an additional degree of freedom representing a kinetic mass[16,17]

$$m_i\frac{d^2\mathbf{r}_i}{dt^2} = -\frac{\partial U}{\partial \mathbf{r}_i} - \eta\mathbf{v}_i, \quad i \in [1,\mathrm{N}] \tag{19}$$

where m_i is the mass of unified atom i, and $\boldsymbol{r}_i$ is the position, $\mathbf{v}_i$ is the velocity, and U is the total potential energy. The evolution of the parameter η is given by

$$\dot{\eta} = \frac{1}{Q}[\sum_i v_i^2 - f] \tag{20}$$

where f is the number of degrees of freedom of the system and Q a kinetic mass.

The numerical integration of eqs 19 and 20 can be performed in many different ways, one common method is the Velocity Verlet algorithm which can be written[18]

$$\mathbf{r}_i(t + \Delta t) = \mathbf{r}_i(t) + \Delta t\mathbf{v}_i(t) + \frac{\Delta t^2}{2}\mathbf{a}_i(t) \tag{21}$$

$$\mathbf{v}_i(t + \Delta t) = \mathbf{v}_i(t) + \frac{\Delta t}{2}[\mathbf{a}_i(t) + \mathbf{a}_i(t + \Delta t)] \tag{22}$$

where $\mathbf{a}_i$ is the acceleration. To use this algorithm in a Nosé−Hoover based MD code it is necessary to rewrite eq 19 as

$$m_i\mathbf{a}_i(t + \Delta t) = -\frac{\partial U(t + \Delta t)}{\partial \mathbf{r}_i} - \eta(t + \Delta t)\mathbf{v}_i(t + \Delta t) \tag{23}$$

Table 1. Input Parameters Used in the Molecular Simulations.

density, $\tilde{\rho}$	temp, $\tilde{\theta}$	cut-off dist, $\tilde{r}_c$	excluded vol param, Λ	kinetic mass, $\tilde{Q}$	spring stiffness, $\tilde{c}_B$
0.85	2	1.4	1	500	800

Inserting this equation into eq 22 results in

$$\mathbf{v}_i(t+\Delta t) = \mathbf{v}_i(t) + \frac{\Delta t}{2}\left\{\frac{-1\partial U(t+\Delta t)}{m_i \quad \partial \mathbf{r}_i} - \frac{\eta(t+\Delta t)}{m_i}\mathbf{v}_i(t+\Delta t) + \mathbf{a}_i(t)\right\} \quad (24)$$

Solving for $\mathbf{v}_i(t+\Delta t)$ gives

$$\mathbf{v}_i(t+\Delta t) = \left[1 + \frac{\eta(t+\Delta t)\Delta t}{2m_i}\right]^{-1}\left\{\mathbf{v}_i(t) - \frac{\Delta t}{2m_i}\frac{\partial U(t+\Delta t)}{\partial \mathbf{r}_i} + \frac{\Delta t \mathbf{a}_i(t)}{2}\right\} \quad (25)$$

The MD procedure then simply becomes the following:

1. Start with a given initial configuration: $\mathbf{r}_i(t)$, $\mathbf{v}_i(t)$, $\mathbf{a}_i(t)$.
2. Calculate $\mathbf{r}_i(t+\Delta t)$ with eq 21.
3. Calculate $\eta(t+\Delta t) = \eta(t) + \Delta t\dot{\eta}(t) + \ddot{\eta}(t)\Delta t^2/2$.
4. Calculate $\mathbf{v}_i(t+\Delta t)$ with eq 25.
5. Calculate $\dot{\eta}(t+\Delta t)$ with eq 20.
6. Calculate $\mathbf{a}_i(t+\Delta t)$ with eq 23.
7. Calculate $\eta(t+\Delta t) = {}^2/_Q\sum \mathbf{v}_i(t+\Delta t)\mathbf{a}_i(t+\Delta t)$.
8. Save data and go to 2.

To start the MD simulation, both the initial velocities and the initial accelerations of all atoms need to be specified. The accelerations can all be taken to be zero, but to get the right kinetic energy and therefore also the temperature, it is sufficient to choose the velocity components v_{ix} from the Gaussian distribution

$$\rho(v_{ix}) = \sqrt{\frac{m}{2\pi k_B \theta}}\exp\left[\frac{-mv_{ix}^2}{2k_B\theta}\right] \quad (26)$$

where $\rho(v_{ix})$ is the probability density for velocity component v_{ix}.

4. Initial Structure

A well-equilibrated initial structure is constructed by randomly generating a melt of all chains. The melt was then allowed to relax for an extended amount of time using a Monte Carlo (MC) method to make the system reach a local energy minimum. The system was then cross-linked using the MC-based cross-linking algorithm described in section 3.

The size of the unit cell used in all simulations was rather small containing only 2×10^4 unified atoms configured into 200 chains; see the schematic representation in Figure 2.

In this figure, the diameter of the atoms has been reduced to make it easier to distinguish the different regions of the system. The input parameters used in the simulations are summarized in Table 1. Results from a representative simulation are presented in Figures 3−8. Figure 3 illustrates that the number of free chains is close to zero and that the number of dangling chain ends is quite small.

The radial distribution function in the undeformed state, plotted in Figure 4, demonstrates a peak at the first nearest neighbor distance. At larger distance the spatial correlation becomes more random, causing $g(r) \rightarrow 1$.

To examine the initial structure of the simulated system, Figure 5 shows the distribution of bond lengths in the undeformed state illustrating that virtually all bonds have a length between 0.9 and 1.1.

The distribution in chain lengths is shown in Figure 6. In this case each chain contained 100 bonds each of length $b = 1$, and the figure shows that the average chain length is 10.24, which is in agreement with the random walk prediction $l0 = b\sqrt{n} = 10$. The figure also depicts the distribution obtained using Gaussian chain statistics (see eq 1) illustrating that the simulated chain length distribution is in good agreement with the statistical mechanics theory.

The distribution in bond angles (the angle between the bond vector and the axial direction) in the undeformed state is presented as a pole figure in Figure 7 demonstrating a uniform random distribution.

Figure 8 shows the distribution in chain angles (the angle between the end-to-end vector of the chain and the loading direction) again demonstrating a random distribution.

As a final evaluation of the initial structure, the Kuhn statistical segment length, $b_k = \langle l^2\rangle/l_{max}$, for the system was calculated to be 1.232. This value is larger than 1 due to excluded volume interactions.

5. Tension Results

A representative volume element (RVE) containing 200 chains is now deformed in tension.[25] Results are presented detailing the evolution in structure and the evolution in stress−strain behavior with deformation.

The applied strain history used in the simulation is shown in Figure 9.

In this case, the RVE was uniaxially deformed in tension to a final true strain of $\epsilon = 0.7$ (a logarithmic strain measure is used), after which the applied deformation was removed with the same rate. In this and the following figures, a dotted vertical line indicates the beginning of a new loading segment. Figure 9 also depicts three bond angle pole figures (looking down the load axis), illustrating the point that during the deformation the bond angles start to become aligned with the loading direction.

The maximum, average, and minimum bond lengths as a function of simulation time are shown in Figure 10 demonstrating that on average the bond lengths are nearly constant with applied deformation.

This is also demonstrated in Figure 11 which shows the average bond force as a function of simulation time.

As shown in the figure, on average the bonds are under a compressive force in agreement with the results from Gao and Weiner.[12] The average bond force is also observed to become less compressive with tensile strain.

The average bond angle as a function of deformation history is shown in Figure 12.

If all bonds are initially randomly oriented the average bond angle is given by

$$\langle\alpha\rangle = \int_0^{\pi/2} d\Theta \int_0^{\pi/2} d\phi \arccos(\cos\Theta\cos\phi)\cos\Theta \approx 57.3°$$

which is in good agreement with the initial state of the simulated system. Figure 12 also shows that even though the RVE is stretched to a true strain of 0.7 (a tensile stretch of 2.0), the average bond angle does not

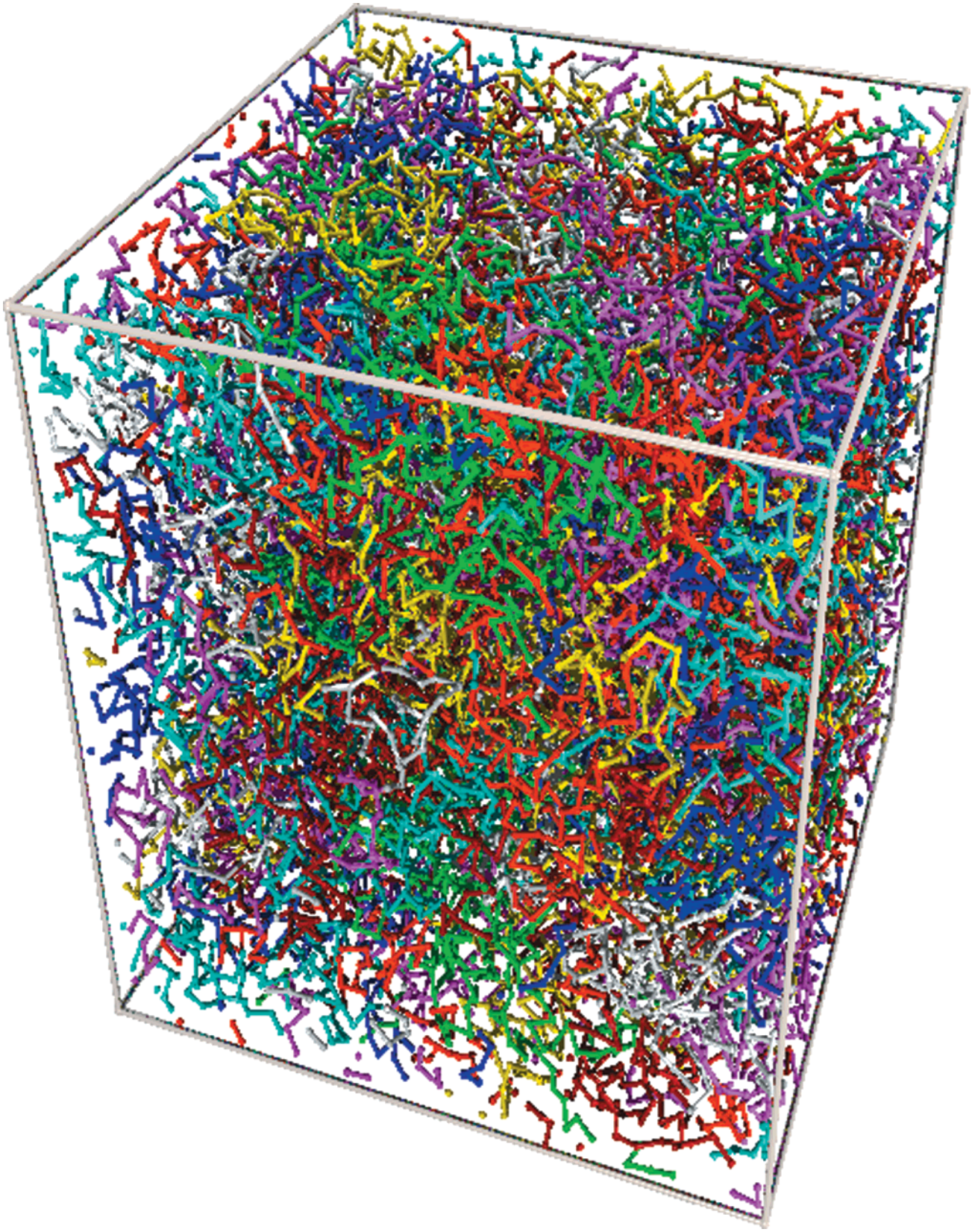

Figure 2. Distribution of atoms in the RVE in the undeformed state, $N = 20\,000$.

change by more than about 6°. When the displacement is reversed, the bond angles rotate back toward their original position but overshoot the initial angle. The effect of this on the stress−strain behavior will be shown later.

The evolution in chain angle with deformation is shown in Figures 13 and 14.

These figures show the evolution in average chain angle (averaged over the 200 chains in the system) as well as the evolution in the chain angle of six individual chains. On average, the network chains are observed to rotate toward the principal stretch direction. The average chain angle evolves in a manner similar to that of the average bond angle; note, however, that the

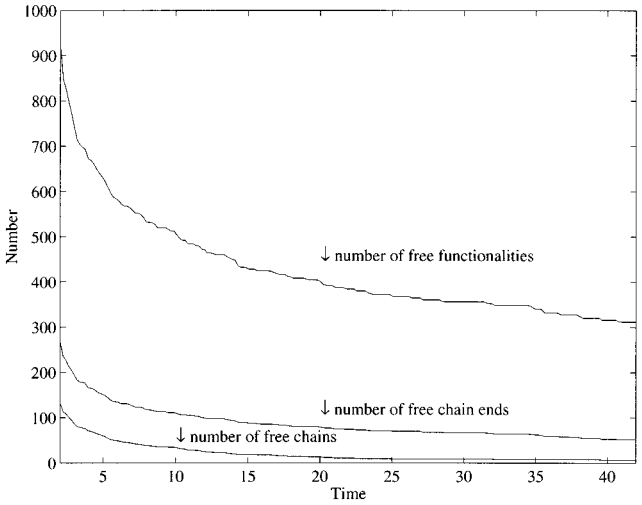

Figure 3. Cross-linking of the RVE as a function of simulation time (MC, 2×10^4 atoms, 200 chains).

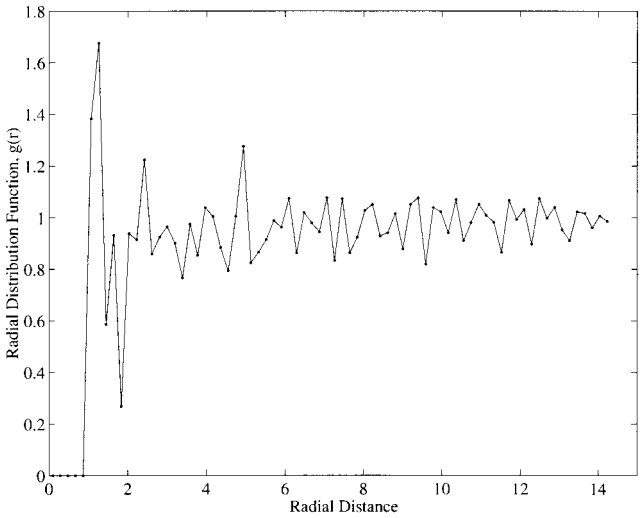

Figure 4. Radial distribution function of the simulated system in the undeformed state.

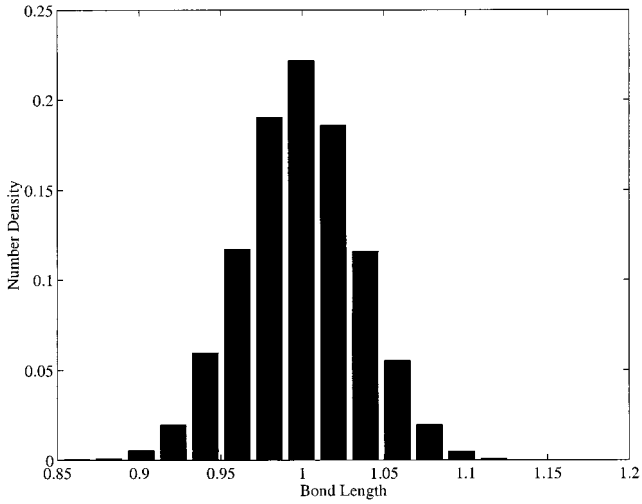

Figure 5. Bond length distribution in the undeformed state.

magnitude of the change of the average chain angle is about 18°, which is significantly larger than the 5° change in average bond angle. This small change in bond angle indicates the freedom of sampling space at the bond level, consistent with Gaussian statistics

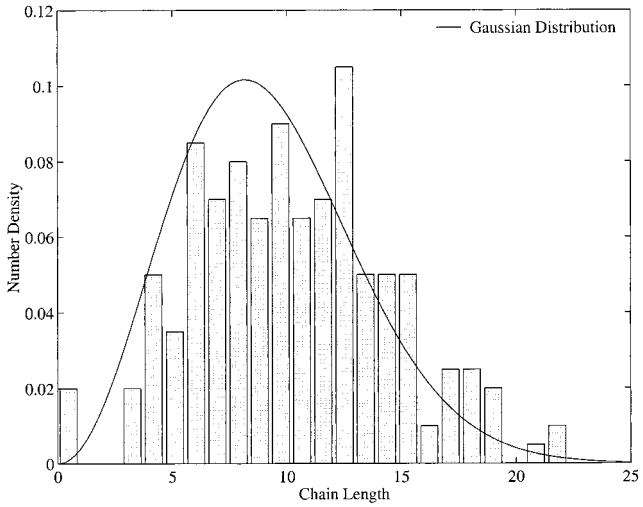

Figure 6. Chain length distribution in the undeformed state.

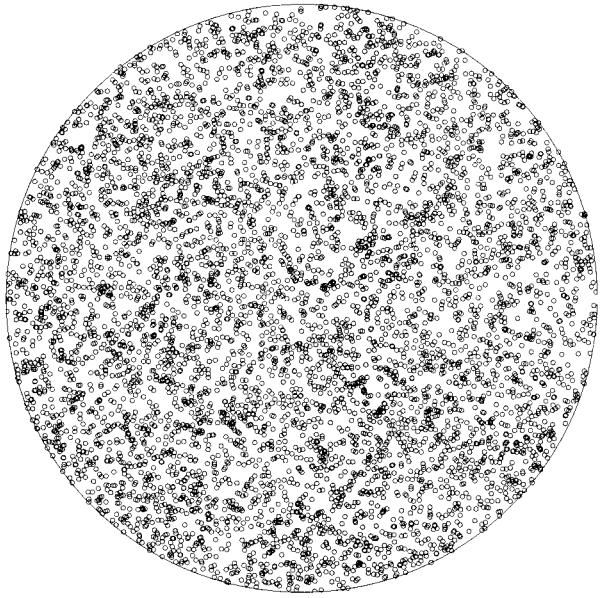

Figure 7. Bond angle pole figure of the initial state of the simulated system.

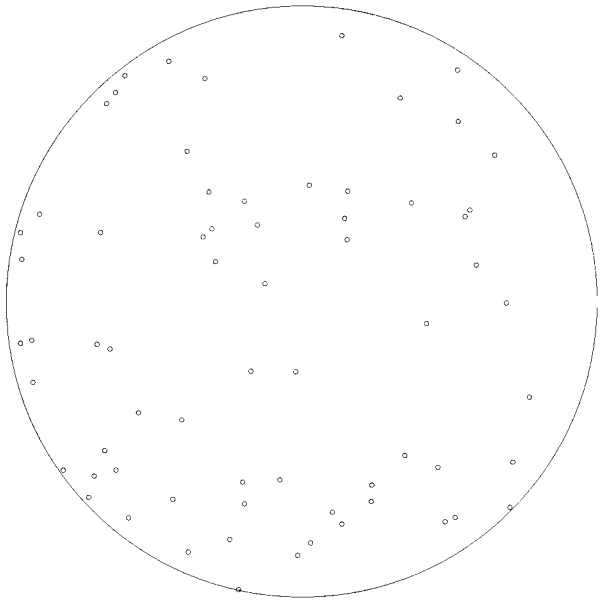

Figure 8. Chain angle pole figure of the initial state of the simulated system.

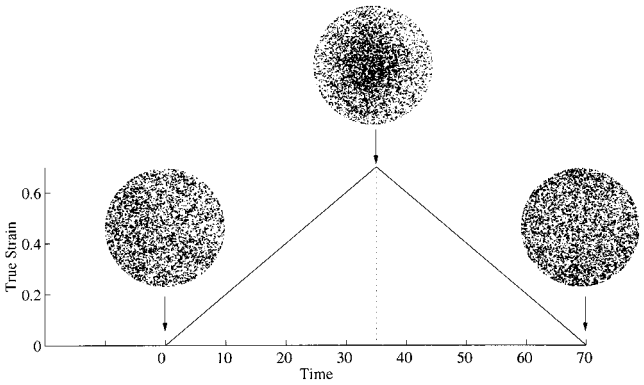

Figure 9. Applied strain history with bond angle pole figures.

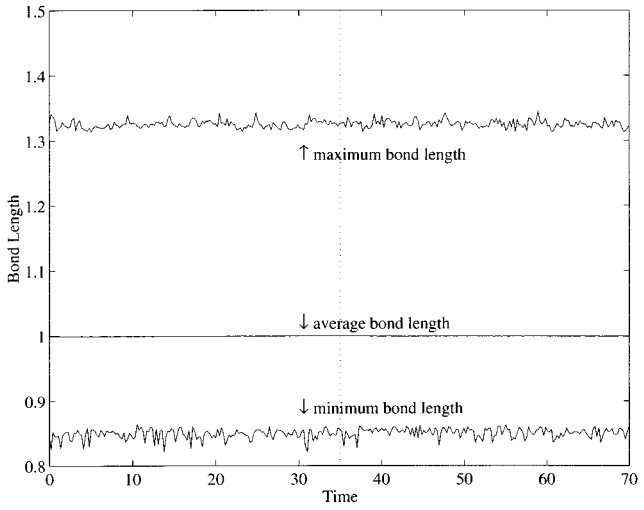

Figure 10. Maximum, average, and minimum bond lengths as a function of simulation time during tensile loading and unloading.

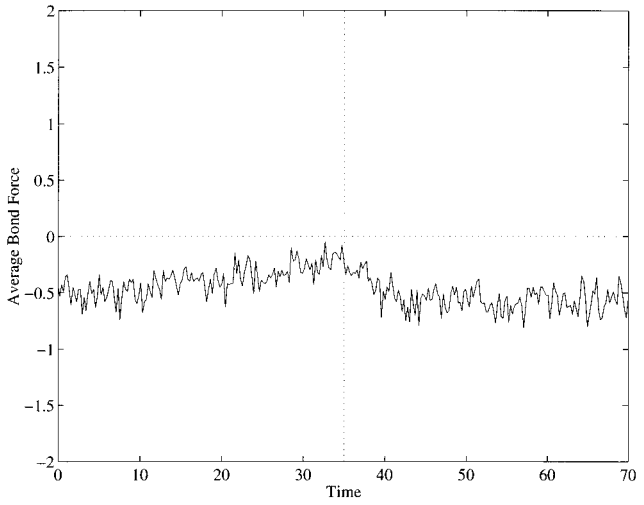

Figure 11. Average bond force as a function of simulation time during tensile loading and unloading.

assumptions (one would anticipate less freedom at larger stretches). At both the initial deformation and the strain reversal point, the average bond angle undergoes a more rapid change than what is observed for the average chain angle. This has direct impact on the macroscopic stress−strain behavior, as will be discussed later.

Figures 15 and 16 depict the evolutions in the end-to-end distances of six individual chains (the evolution

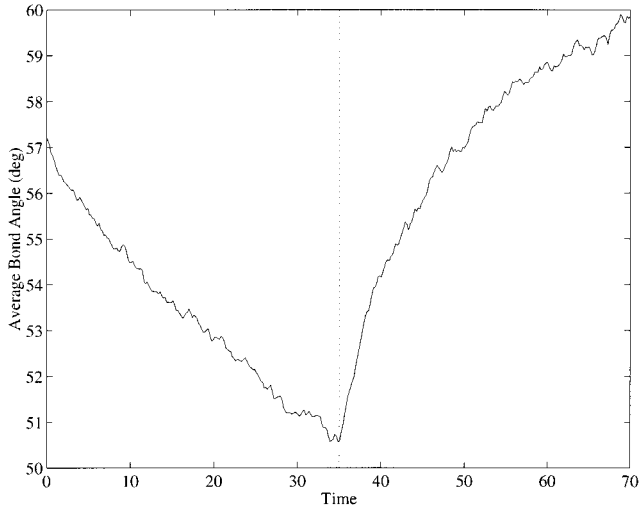

Figure 12. Average bond angle of all bonds as a function of simulation time during tensile loading and unloading.

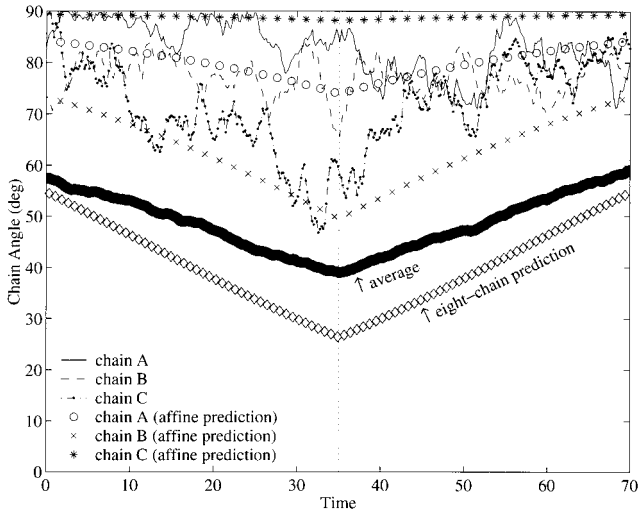

Figure 13. Chain angles as a function of simulation time during tensile loading and unloading.

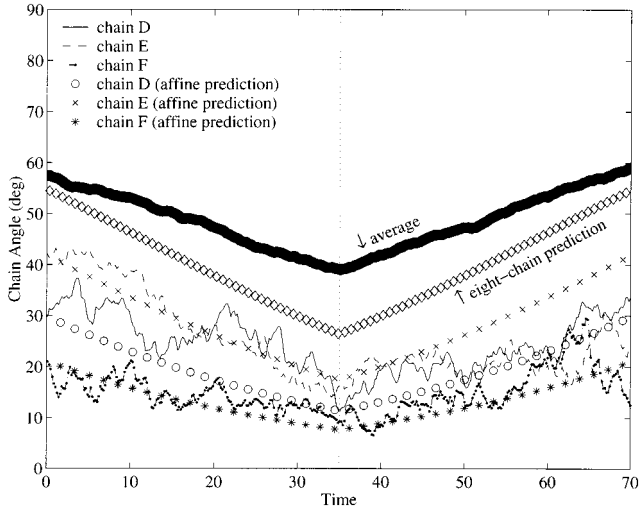

Figure 14. Chain angles as a function of simulation time during tensile loading and unloading.

in chain angle for these same chains was reported earlier in Figures 13 and 14).

Chains which are more closely aligned with the tensile stretch axis (chains D, E, and F in Figures 14

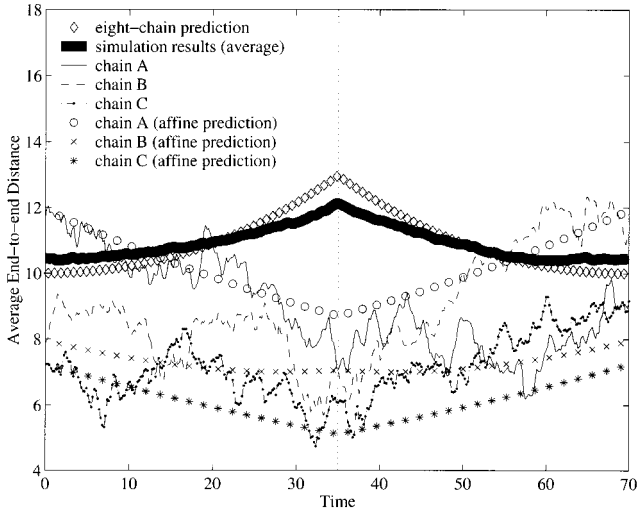

Figure 15. Chain end-to-end distance as a function of simulation time during tensile loading and unloading.

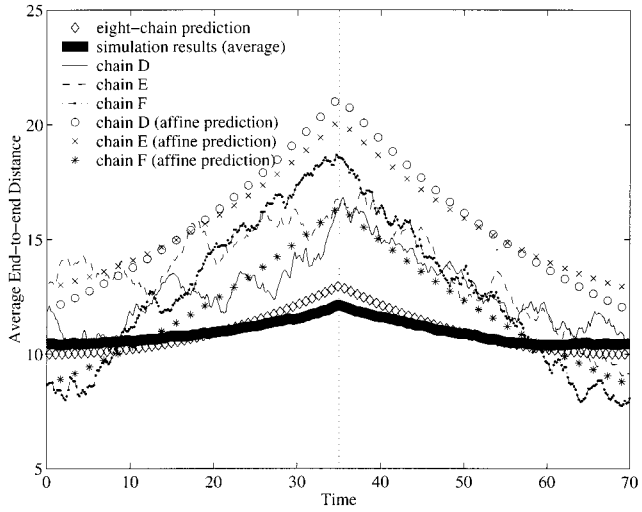

Figure 16. Chain end-to-end distance as a function of simulation time during tensile loading and unloading.

and 16) are found to stretch as well as to rotate toward the tensile axis. It is clear that, at any increment in the deformation, these individual chains undergo large fluctuations in end-to-end distance and angle, but each tends toward stretching and rotating toward the principal stretch direction. Chains which are initially nearly orthogonal to the tensile axis (chains A and B in Figures 13 and 15) are not found to stretch and, in some cases, to even reduce the end-to-end distance.

Figures 13−16 also include the affine deformation prediction of the behavior of the six randomly selected chains as well as the eight-chain network model prediction of the effective network chain behavior. As discussed in section 2, the eight-chain model possesses chains that lie along the diagonals of the cell; these chains will stretch and rotate with the deformations of the cell. For the case of uniaxial deformation, the stretch of the representative chains is given by

$$\lambda_{\text{chain}} = \sqrt{\frac{\lambda^2 + 2/\lambda}{3}} \tag{27}$$

and the end-to-end distance is thus

$$l = \lambda_{\text{chain}} l_0 \tag{28}$$

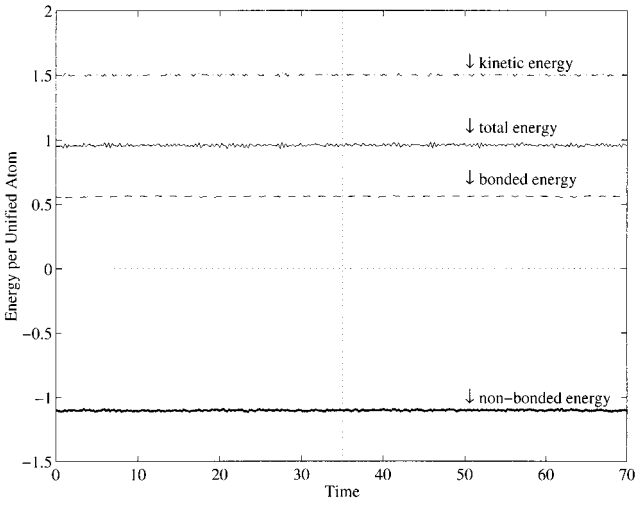

Figure 17. Energies of the RVE as a function of simulation time during tensile loading and unloading.

The chain angle is

$$\beta = \text{acos}\left[\frac{\lambda}{\sqrt{\lambda^2 + 2/\lambda}}\right] \tag{29}$$

Figures 13−16 show the individual chains to deform in a somewhat affine manner. While the chain end-to-end lengths and angles do not evolve in a monotonic manner in the MD simulations, the trend is to follow the affine deformation result for these moderate stretches. Chains D and E are found to rotate in an affine manner but also to stretch considerably less than predicted by affine assumptions; this is perhaps due to their relatively extended initial lengths—early indication of less affineness and the beginning of "non-Gaussian" behavior. The MD computed average chain end-to-end length and angle are found to compare favorably with the eight-chain model predictions where the averaged chain is stretching and rotating toward the principal stretch direction similar to that predicted in the eight-chain model. These comparisons would be interesting to pursue into the non-Gaussian larger stretch region to observe the breakdown in affine deformation of all chains and the apparent robustness of the eight-chain effective network representation in this regime.

So far the discussion has been limited to topological properties of the molecular network, but from the simulation it is possible to study a number of other quantities as well. The variation in the different energy quantities as a function of simulation time is shown in Figure 17 illustrating that the kinetic, bonded, and nonbonded energies all stay virtually constant during the simulation.

This observation is in agreement with traditional rubber elasticity theory in which the deformation resistance is entropy-based.

The variation in the pressure on the lateral sides of the RVE as a function of simulation time is shown in Figure 18.

Since the MD simulation is run at constant volume, the pressure varies with deformation state, but as shown in the figure, the change in lateral pressure is relatively small compared to its overall level. Simulations comparing $NV\theta$ with NVP show nearly identical results[19] in terms of structure and stress−strain behavior.

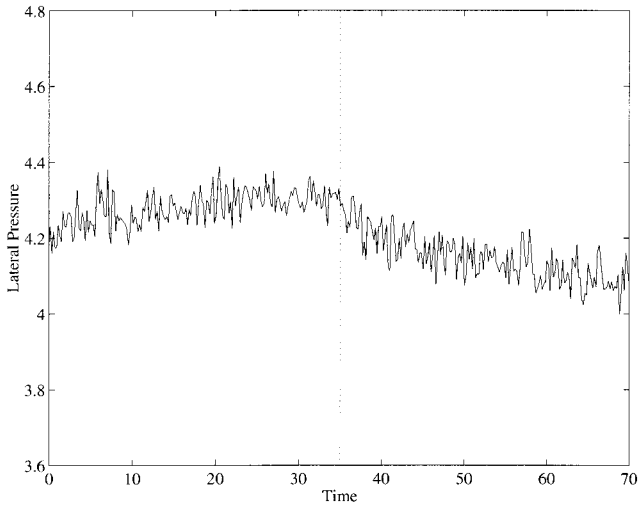

Figure 18. Lateral pressure $(T_{yy} + T_{zz})/2$ in the RVE as a function of simulation time during tensile loading and unloading.

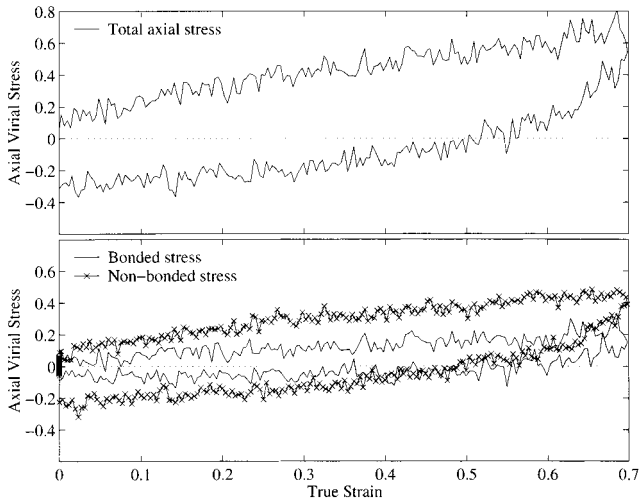

Figure 19. Stress−strain response of the RVE during tensile loading and unloading.

Figure 19 shows the simulated stress−strain response illustrating the same qualitative features that are observed in traditional experimental mechanical tests: the tangent modulus is initially a decreasing function of strain but soon becomes relatively constant (as long as the strain is not too large such that the limited chain stretch is approached), and at the strain reversal there is a significant drop in stress, causing a hysteretic energy loss. Note that the relatively stiff initial response as well as the initial stiff unloading response correlates with a rapid change in bond angle shown earlier in Figure 12.

Figure 19 also depicts the bonded and nonbonded contributions to the stress. Both are observed to increase with strain. The nonbonded stress contributes roughly twice as much to the total stress (at all strain levels) than the bonded stress.[26] The bonded contribution shows significantly less hysteresis during unloading than the nonbonded contribution.

Figure 20 depicts the decomposition of the unmodified stress components. The unmodified axial stress (T_{xx}) is found to contain equal contributions from the bonded and nonbonded sources where the bonded contribution originates from the bonds rotating toward the principal stretch direction. The lateral stresses arise from non-

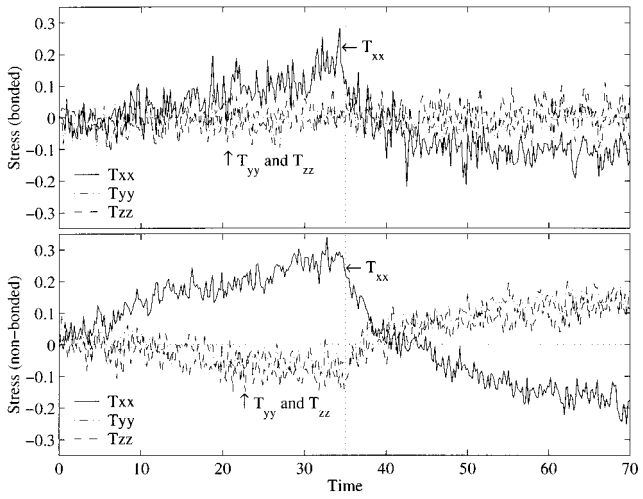

Figure 20. Decomposition of the stress into bonded and nonbonded contributions during tensile loading and unloading.

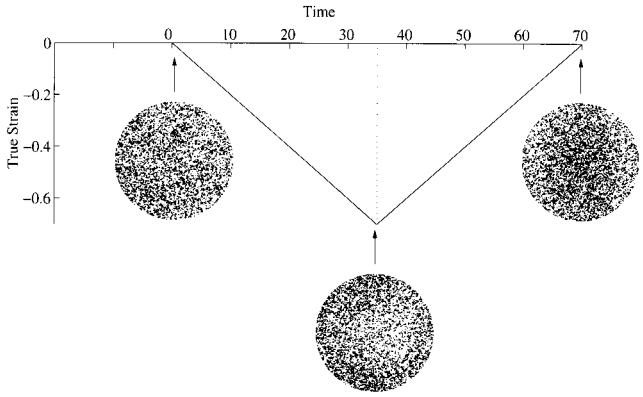

Figure 21. Applied strain history with bond angle pole figures.

bonded contributions due to the constant volume constraint. Note that in this figure all stress components have been vertically shifted so that they start from zero. This procedure allows for a more direct comparison between the changes in magnitudes of the different stress components.

Note that the stress computation is not compared to the stress that would be computed from equilibrium rubber elasticity theories. The MD simulation clearly displays high rate effects on the stress computation as evidenced by the hysteresis observed during unloading. Interestingly, MD simulations of stress relaxation find the chain angles and lengths of the structure to evolve with strain but remain static with time at fixed strain. However, the bond angles we found to evolve with both strain and time. This is consistent with proposed continuum level constitutive models for time-dependent behavior of elastomers[9] and is discussed further in the appendix.

6. Compression Results

A representative volume element (RVE) containing 200 chains is now deformed in compression to a final strain of −0.7. To allow for a direct comparison between the tension and compression simulations the same deformation rate was chosen as in the previous section; see Figure 21.

The distribution of the bond angles in the simulation cell is presented in the bond angle pole figures shown

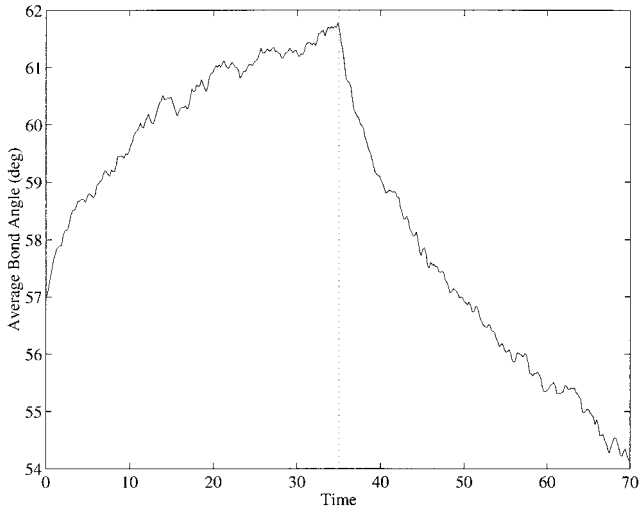

Figure 22. Average bond angle of as a function of simulation time during compressive loading and unloading.

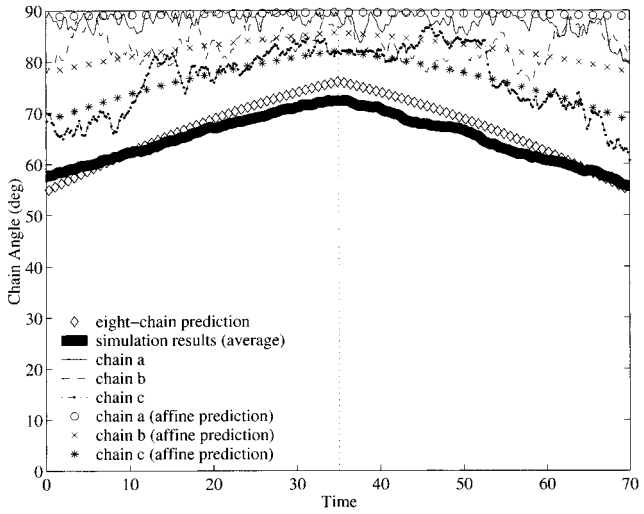

Figure 23. Average end-to-end angle for three chains during compressive loading and unloading.

in Figure 21. From the pole figures it is clear that during the compression segment the average bond angle increases since on average the bonds rotate away from the loading axis. This is further demonstrated in Figure 22 where the average bond angle is shown to be a strong function of the applied deformation.

As in the tension case, the average bond angle only undergoes a relatively small change during the deformation; in this case, the average angle increases about 5° when the RVE is compressed to a true strain of −0.7. Also similar to the tension case is the rapid change in bond angles at the strain reversals and the overshoot in bond angles at the end of the deformation cycle.

Figures 23 and 24 depict the evolution in chain angle with deformation for six randomly selected chains as well as the corresponding evolution in the average chain angle; similarly, Figures 25 and 26 depict the evolution in chain end-to-end length for the same six chains as well as the averaged (over all 200 chains) behavior. Chains initially nearly orthogonal to the loading axis (chains a, b) are found to remain orthogonal and stretch with the deformation; a chain initially at 70° is found to rotate away from the loading axes toward the principal stretch direction and to stretch. Chains initially oriented at angles less than 45° to the loading axis

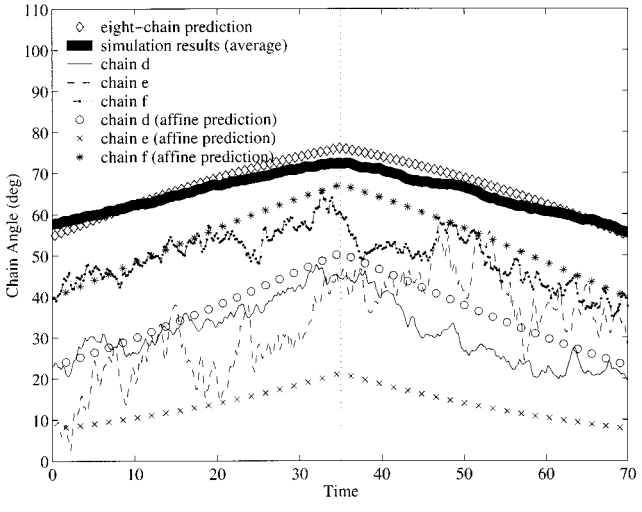

Figure 24. Average end-to-end for three chains during compressive loading and unloading.

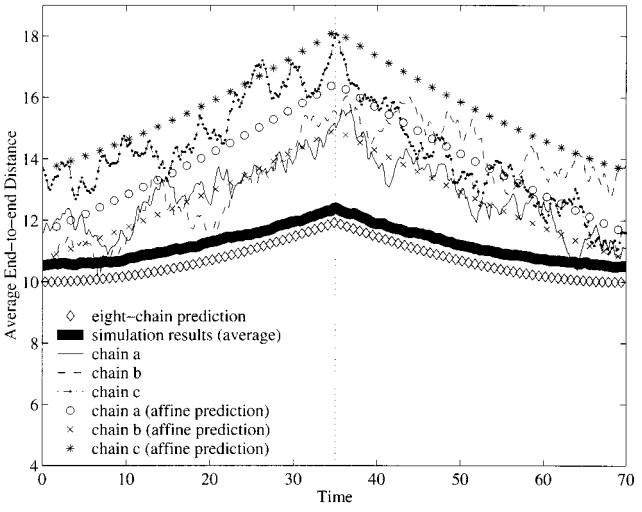

Figure 25. Average chain stretch for three chains during compressive loading and unloading.

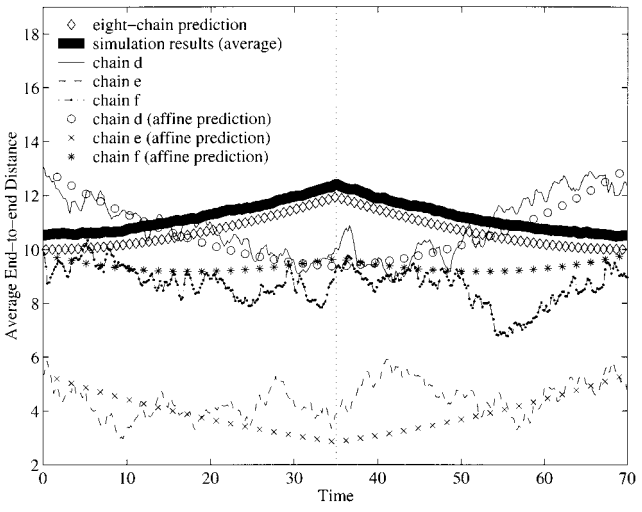

Figure 26. Average chain stretch for three chains during compressive loading and unloading.

are observed to rotate away from the loading axis toward the maximum principal stretch direction and their lengths are found to remain relatively constant or to even decrease with the applied strain. While the individual chains exhibit the basic trend just discussed,

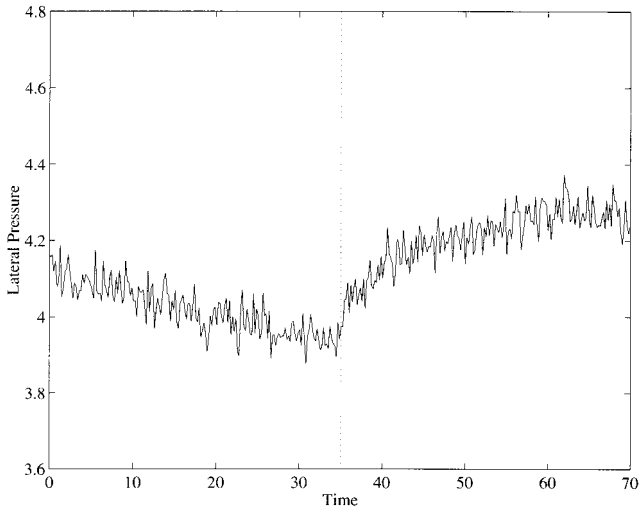

Figure 27. Lateral pressure in the RVE as a function of simulation time during compressive loading and unloading.

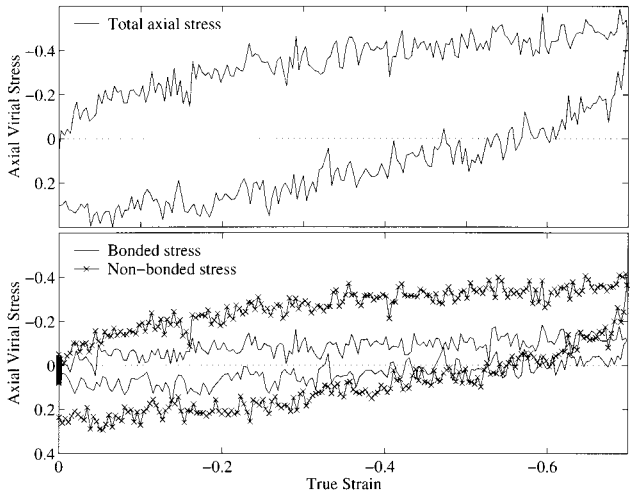

Figure 28. Stress−strain response of the RVE during compressive loading and unloading.

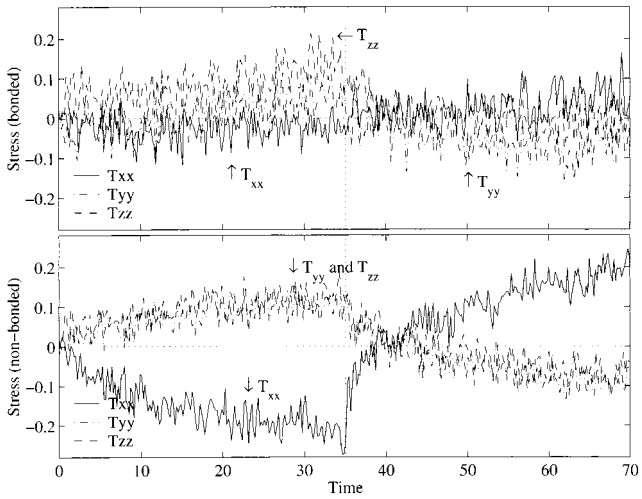

Figure 29. Decomposition of the stress into bonded and nonbonded contributions during compressive loading and unloading.

we note that the behavior is not monotonic but exhibits sudden increases/decreases in chain angle and length as deformation is monotonically increased.

The averaged chain behavior is found to monotonically stretch with applied strain and to monotonically rotate toward the maximum principal stretch direction away from the loading direction.

Figures 23−26 also depict the individual chain behaviors predicted assuming affine deformation of all chains; the eight-chain model is used to predict the averaged or effective chain behavior. The individual chains are found to basically follow the affine deformation assumption. The averaged chain behavior is found to be in excellent agreement with the eight-chain model predictions, suggesting that the eight-chain model does capture an effective network response, and this appears to be the reason for its success (again, this would be interesting to probe into the large strain non-Gaussian regime of behavior).

The variation in lateral pressure (Figure 27) is similar to the tension case. In compression, the lateral pressure decreases a small amount, whereas in tension the lateral pressure had increased a small amount with strain (in both cases about 2.5%). These changes in lateral pressure, although small, indicate that the simulated material is not incompressible.

The compressive stress−strain behavior is shown in Figure 28 and decomposed into bonded and nonbonded contributions in Figure 29.

The stress−strain behavior is similar in character to that obtained earlier in tension. The stress decomposition shows a strong bonded contribution to the lateral stresses since the bonds are rotating toward these directions whereas the unmodified axial stress (T_{xx}) is dominated by nonbonded contributions.

7. Conclusions

In polymer science, molecular dynamics (MD) or Monte Carlo (MC) simulations are becoming important tools for understanding structure property relationships. In this work, it has been demonstrated that molecular simulations can be a useful tool for studying the mechanical behavior of elastomeric networks. By comparing results from MD simulations in both compression and tension it has been shown that this type of simulation can produce results that are in good qualitative agreement with experimental data. A number of interesting observations are directly obtained from the simulations. For example, the simulations clearly demonstrate a very strong correlation between the average bond angle and the stress in the system. This observation does not seem to be very well documented in the literature, but can easily be understood in terms of the virial stress theorem.[21] The change in average bond angle with applied deformation is further shown to be relatively small: applying a true strain of ±0.7, for example, only causes a change in the average bond angle of about ±6°. Similarly the change in chain angle with applied deformation is also shown to be small. Here, applying a true strain ±0.7 causes a change in chain angle of about ±18°. This observation is in good agreement with the prediction from the eight-chain model.[6] From the simulations, it is also possible to follow the average chain stretch as a function of applied deformation. It is interesting to note that the average chain stretch only becomes about 1.2 when the applied stretch is 2. This observation is also in good agreement with the eight-chain model. The simulations have also indicated that both in tension and compression the chains deform in a somewhat affine manner.

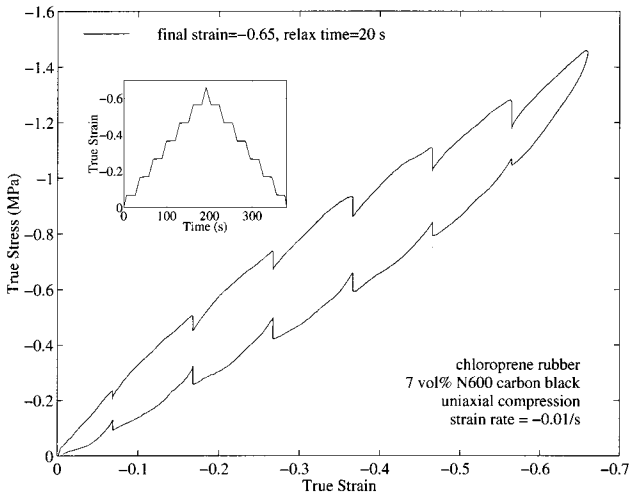

Figure 30. Experimental stress−strain data for chloroprene rubber.

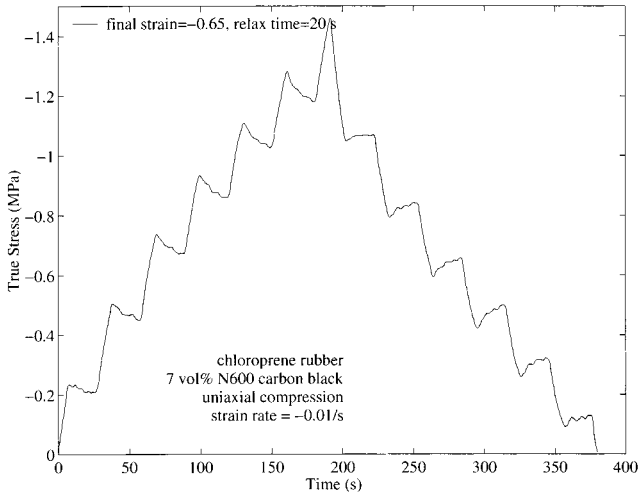

Figure 31. Experimental stress−time data for chloroprene rubber.

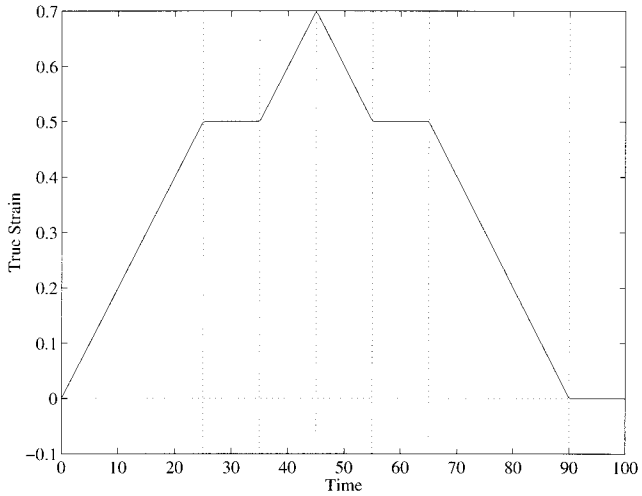

Figure 32. Applied strain history in the stress relaxation simulation.

Since the energy of the system consists of two parts, bonded and nonbonded contributions, it is possible to decompose the total stress into contributions from those two interactions. Results from this decomposition indicate that the bonded component contributes to the stresses in the principal stretch directions since the bonds rotate toward the maximum principal tensile stretch; the nonbonded component contributes in all directions as they act to maintain the volume and balance the bonded stress.

In conclusion, molecular simulations of the type used in this work are an interesting complement to traditional experiments when developing constitutive equations. It is particularly interesting to see how many features of the simulation results are universal, which do not depend on the particular techniques or parameters used in the simulations, and the very good qualitative agreement with experimental data. In a future study it would be interesting to extend the work presented here to include also a more careful investigation of different cross-linking densities and time-dependent effects as well as studying large deformations where the limited stretch of the chains is approached thus enabling a test of inverse Langevin statistics.

Acknowledgment. This research was funded, in part, by the US NSF through Grant No. CMS-9622526 and through the NSF MRSEC MIT CMSE through Grant No. DMR-98-08941.

Appendix A. Stress Relaxation Simulation

One common method to characterize both equilibrium and time-dependent behavior of elastomeric materials is to run mechanical compression tests of the type shown in Figures 30 and 31.

These two figures show the response of a chloroprene rubber subjected to the strain history shown in the inset of Figure 30.[9] As indicated in the figures, during constant strain rate loading the magnitude of the stress is monotonically increasing, but if the strain is held constant, the stress starts to relax toward an equilibrium value.

The same technique can be used to examine both the equilibrium and time-dependent behavior of the simulated polymer network. One example loading history that has been used here is shown in Figure 32. In this case, the strain was held constant for a normalized simulation time of 10 when it reached a value of 0.5, during both loading and unloading. In addition, the strain was also held constant after the load cycle was completed.

The evolution in average bond angle with simulation time is illustrated in Figure 33. From the figure it is clear that the average bond angle overshoots its equilibrium value during both loading and unloading and that during the relaxation segments the average bond angle starts to approach the strain-dependent equilibrium value.

The evolution in chain angle with deformation is shown in Figure 34, illustrating that the average chain angle evolves similar to what is predicted from the eight-chain model. In particular, it remains relatively constant during the stress relaxation segments.

Figure 35 depicts the evolution in the end-to-end distance of the same three individual chains shown in Figure 34. As shown in the figure, the average chain end-to-end distance is close to the prediction from the eight-chain model.

Figure 36 depicts the total axial stress as a function of simulation time. It is clear that behavior of the simulated network is qualitatively very similar to the characteristic behavior that is seen in real experiments.

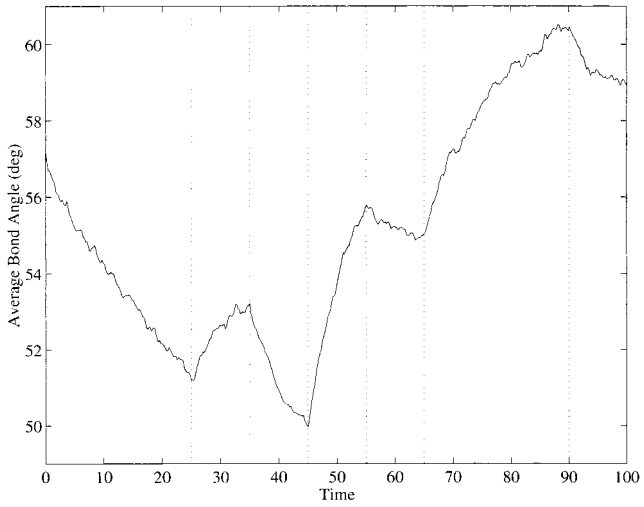

Figure 33. Average bond angle as a function of simulation time.

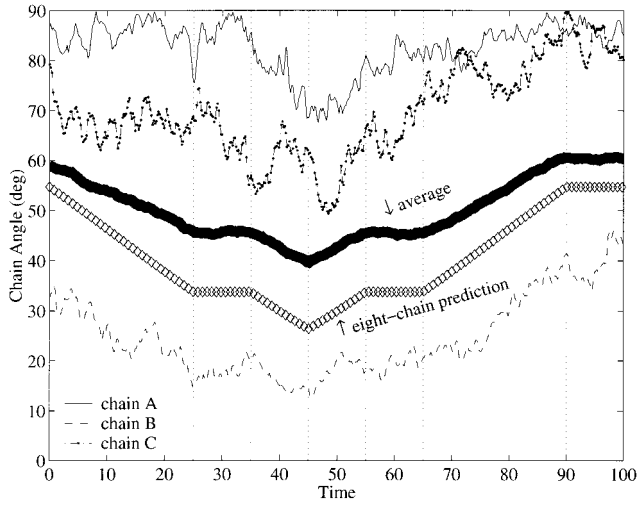

Figure 34. Chain angles as a function of simulation time.

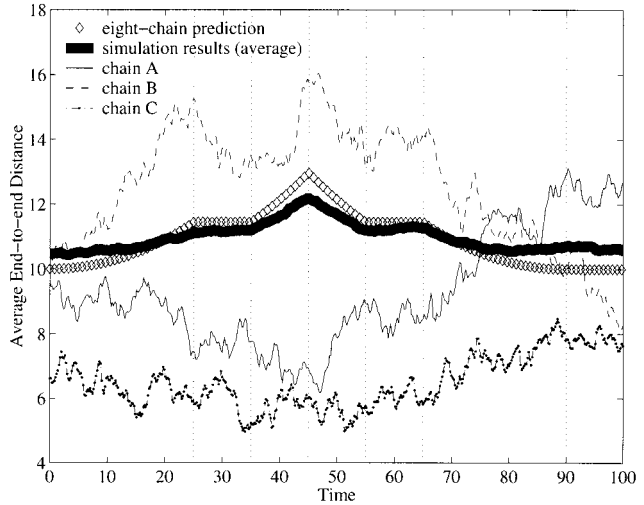

Figure 35. Chain end-to-end distance as a function of simulation time.

The deviation between the uploading and unloading behavior of the simulated network is due to the high deformation rate relative to the relaxation times of the network, exactly the same reason the experimental data in Figures 30 and 31 does not coincide with the equilibrium behavior. The equilibrium behavior of the simulated network can be estimated by considering both the behavior during uploading and unloading.

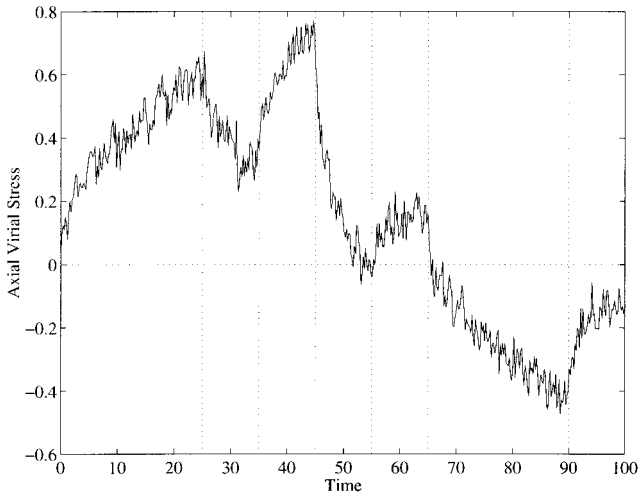

Figure 36. Axial stress as a function of simulation time.

References and Notes

(1) Treloar, L. R. *The Physics of Rubber Elasticity*; Oxford University Press: Oxford, England, 1975.
(2) Wall, F. T. *J. Chem. Phys.* **1942**, *10*, 485.
(3) Treloar, L. R. G. *Trans. Faraday Soc.* **1943**, *39*, 241.
(4) Kuhn, W.; Grün, F. *Kolloid Z.* **1942**, *101*, 248.
(5) Wang, M. C.; Guth, E. J. *J. Chem. Phys.* **1952**, *20*, 1144.
(6) Arruda, E. M.; Boyce, M. C. *J. Mech. Phys. Solids* **1993**, *41*, 389.
(7) Treloar, L. R. G. *Trans. Faraday Soc.* **1954**, *50*, 881.
(8) Wu, P. D.; van derGiessen, E. *J. Mech. Phys. Solids* **1993**, *41*, 427.
(9) Bergström, J. S.; Boyce, M. C. *J. Mech. Phys. Solids* **1998**, *46*, 931.
(10) Chui, C.; Boyce, M. C. *Macromolecules* **1999**, *32*, 3795.
(11) Gao, J.; Weiner, J. *Macromolecules* **1987**, *20*, 2520.
(12) Gao, J.; Weiner, J. H. *Macromolecules* **1989**, *22*, 979.
(13) Verlet, L. *Phys. Rev.* **1967**, *159*, 98.
(14) Hockney, R. W.; Goel, S. P.; Eastwood, J. W. *J. Comput. Phys.* **1974**, *14*, 48.
(15) Duering, E. R. *J. Chem. Phys.* **1994**, *101*, 8169.
(16) Nosé, S. *Mol. Phys.* **1984**, *52*, 255.
(17) Hoover, W. G. *Phys. Rev. A* **1985**, *31*, 1695.
(18) Allen, M. P.; Tildesley, D. J. *Computer simulation of liquids*; Oxford University Press: Oxford, England, 1987.
(19) Bergström, J. S. Large Strain Time-Dependent Behavior of Elastomeric Materials. Ph.D. Thesis, MIT, 1999.
(20) Gao, J.; Weiner, J. H. *Macromolecules* **1991**, *24*, 1519.
(21) Picu, R. C.; Loriot, G.; Weiner, J. H. *J. Chem. Phys.* **1999**, *110*, 4678.
(22) Clearly, it would be of interest in future work to parametrically study the effect of bending and torsional potentials on the structure and its evolution with deformation.
(23) Note that, although this potential is continuous, its gradient is not continuous. This, however, does not cause any problems in the large scale simulations used in this work in which long-term statistical averages are the main interest.
(24) When calculating the stress the standard tail correction term was used: $P^{\text{tail}} = 16\pi\rho^2(2r_c^{-9}/3 - r_c^{-3})/3$.
(25) Note that simulations on a single chain model of 20 000 atoms (no cross-links) yield similar results in terms of evolution in bond orientation and stress with strain.[19]
(26) Note that Gao and Weiner[20] also find the nonbonded component to be dominant in their study on oriented melts; however, surprisingly, they find the bonded contributions to be negative.

MA0007942